Structural and diffusional phase transformations in liquid-quenched MgYZn ribbons below the bifurcation temperature

Okuda, Hiroshi; Yamasaki, Michiaki; Kawamura, Yoshihito

Acta Materialia 194 (2020) 587_593

https://doi.org/10.1016/j.actamat.2020.05.048

Structural and diffusional phase transformations in liquid-quenched $Mg_{85}Y_9Zn_6$ ribbons below the bifurcation temperature

Hiroshi Okuda[1], Michiaki Yamasaki[2] and [2]Yoshihito Kawamura[2]

1. Department of Materials Science and Engineering, Kyoto University, Yoshida-Honmachi Sakyo-ku, Kyoto 606-8501 Japan
2. Department of Materials Science, Kumamoto University, Kurokami, Kumamoto 860-8555, Japan

Abstract:

In-situ and simultaneous small- and wide-angle scattering measurements of liquid-quenched $Mg_{85}Y_9Zn_6$ alloy ribbons were performed to examine phase transition during isothermal annealing at the temperatures below the bifurcation temperature, where long-period stacking ordered (LPSO) structures are not formed yet in the previous work. Even below the temperature, sluggish structural transformation destroying hcp stacking sequence was observed, and development of in-plane and interplane cluster structures, as imperfect LPSO structure, became noticeable at long time annealing. The characteristic time for structural transformation showed well-defined thermally activated process with Q=173.3 +/- 14.4 kJ/mol.

Keywords,

Small- and wide- angle X-ray scattering (SWAXS)

Synchrotron Radiation

Phase transformation kinetics

Mg alloy

Stacking fault

Corresponding author

Hiroshi Okuda,

Department of Materials Science and Engineering,

Kyoto University,

Yoshida-Honmachi, Sakyo-ku Kyoto 606-8501 Japan

Email: okuda.hiroshi.5a@kyoto-u.ac.jp

Tel. +81-75-753-5193

1.Introduction

Mg alloys have advantages of their superior specific weight over other structure materials. A group of Mg alloys containing long-period stacking ordered (LPSO) structures[1-4] was found to show excellent potential on some of the drawbacks that conventional Mg alloys had[1,5,6]. MgYZn alloys, which are representative alloys in a sense that they are the first alloys found to show the LPSO structures, and also indicated excellent potential for structural materials use[1-5]. Intensive researches have been made to unveil the structural details of the LPSO structures using TEM [7-9], first principles calculations [10,11], and phase diagram approaches [12,13]. Although annealed stoichiometric samples gave fully ordered structures[14,15], samples with intermediate compositions or annealing conditions showed looser and disordered in-plane arrangements of clusters, while the clusters themselves remain the same[16]. Therefore, from a viewpoint of static structure, the LPSO structure is hierarchical, with $L1_2$ clusters as a lower hierarchy and the spatial arrangements of such clusters as an upper hierarchy[17] . The composition used in the present study, Mg-9at%Y-6at%Zn alloy, hereafter referred as $Mg_{85}Y_9Zn_6$, is known to have a single phase 18R LPSO microstructure after long-time annealing [3,6].

From a kinetic viewpoint, in-situ examinations using amorphous $Mg_{85}Y_9Zn_6$ ribbons [17,18] revealed that the clustering occurs first in amorphous and hcp crystals, and when the size of clusters grew to reach the size of so-called $L1_2$ cluster in LPSO structures, introduction of stacking faults as observed by the decrease in the integrated intensity of hcp 103 Bragg peak became remarkable [18]. Therefore, the introduction of stacking faults became noticeable when the average size of the clusters matured to the size of what is observed in the well-ordered LPSO structures. Figure 1 shows the change of the SAXS and the WAXD patterns of $Mg_{85}Y_9Zn_6$ redrawn from [17,18] as a two-dimensional color map of temperature versus scattering vector and the change of the

integrated intensity of 103 Bragg peak during heating at 10 K/min. The results suggested that the transition from supersaturated hcp state to heavily stacking-faulted structure leading to 18R-LPSO became notable at a temperature as measured by the decrease of integrated intensity of 103 hcp Bragg peak [17,18]. This transition accompanied the change in the nearest-neighbor distance of $L1_2$ clusters from an average distance into two kinds of nearest-neighbor distances, if the in-plane and the out-of-plane distances [17,19], namely, the bifurcation of nearest neighbor distance of clusters was observed. We may call the temperature the bifurcation temperature, T_{bif}, determined by the integrated intensity as shown in Fig. 1. Concerning the structural transformation, Iikubo et al.[20] discussed the lattice instability temperature using first principles calculations that can be athermal, while Kiguchi et al.[21,22] and Kim et al.[23] showed early stage of growth of the defects developing concomitant with segregation in dilute alloys. Therefore, it should be worthwhile examining the kinetics of the structural transformation process in the alloys from an isothermal transformation viewpoint.

2. Experimental

We performed in-situ and simultaneous small- and wide- angle scattering (SWAXS) measurements on the isothermal transformation process in $Mg_{85}Y_9Zn_6$ alloys. Figure 2 shows a schematic temperature diagram used in the present in-situ experiments. To compare the present isothermal results with the previous works [17,18], we used the heating condition of 10 K/min up to the melting point described above as the reference. The SWAXS measurements have been performed at BL45XU of SPring8 and BL6A of Photon Factory, Japan. The sample preparation and the SWAXS apparatus used in the present work are the same as the previous ones [17-19]. In the present experiments, an isothermal annealing process at T_A started when the sample temperature reached T_A

during heating amorphous ribbons. Amorphous ribbons are kept in graphite sheet envelope and heated up to the isothermal temperatures under vacuum. Time-resolved SAXS and WAXD measurements were made simultaneously using Pilatus 1M/2M for SAXS and Pilatus 100K for WAXD.

3. Results and Discussions

3.1 Difference in SWAXS patterns between constant rate heating and isothermal heating.

During heating at 10 K/min., crystallization occurs at T_x, which was clearly seen by appearance of hcp 103 diffraction peak as marked by a green triangle on the WAXD map in Fig.1, and it disappears at T_{bif} when the SAXS peak from the clusters start to split into two peaks as shown in Fig.1 [18]. In the present work, the temperatures between T_x and T_{bif} were chosen for isothermal annealing. Figure 3 gives an example of the temperature-scattering vector viewgraph of SAXS and WAXS intensity profiles for the isothermal annealing. It shows that for SAXS profile, a peak slowly grows with time even after annealing for 2 hours, in contrast to a clear bifurcation observed very soon for the constant rate heating. For WAX part, the 103 peak decreased slowly during isothermal annealing, although the annealing temperature is well below the bifurcation temperature, but was still present after 1.5 hours of annealing. Therefore, the introduction of stacking fault occurs under the isothermal condition at lower temperatures between T_x and T_{bif}. However, new diffraction peaks representing long-range stacking order of 18R as marked by the red diamonds at higher temperatures in constant rate heating do not appear in the WAXD map for isothermal annealing. This suggests that the stacking faults are densely introduced during isothermal annealing, yet the sequence of the stacking is rather random and diffraction peaks originating from long-range stacking order is not observed. We may call this short-range stacking ordered (SR-SO) state, which is a nonequilibrium microstructure appearing transiently by kinetics of phase transformation.

Figure 4(a) shows temporal evolution of SAXS profiles during isothermal annealing at 510 K. The profiles have two main components, the very strong one at smaller q below 2 nm^{-1}, which are

mainly explained by the scattering from grains caused by segregation [18], and the other one at higher q between 3 nm^{-1} and 7 nm^{-1} which are due to scattering from clusters [17,18]. To examine the latter, the SAXS component from crystallites was subtracted from the intensity before analyzing the cluster component. From the amorphous state to the beginning of isothermal annealing, the SAXS profiles from clusters show single peak scattering profiles. For longer annealing time, however, the profiles split into two broad peaks as indicated by the arrows in the figure. The peak at lower q moves towards 4 nm^{-1} corresponding to the distance between stacking faults / segregation layers of LPSO, since the peak position of 18R are known to appear at 4 nm^{-1}[24]. The other peak is the inter-cluster distance in the segregation layers. Compared with the SAXS peaks cast $Mg_{85}Y_9Zn_6$ alloys[24], notable difference is that the peak corresponding to the periodicity of segregation layers remained much weaker and broader, and the peak position is slightly different from the exact 18R position of 4 nm^{-1}. Therefore, the process rather suggest random introduction of stacking faults, with the average spacing of segregated layers being slightly denser than that for 18R, i.e., every 6 atomic layers, and clusters become more likely to stay on stacking faults. The 103 peak shown in Fig.4(c) shows that well-defined 103 peak, i.e. hcp stacking regions still survives after 5 ks of isothermal annealing. Typical microstructure of randomly introduced stacking sequence is achieved for the microstructures observed in the constant rate heating in Fig.1 for the temperature range between T_{bif} and $T_{LR,}$ where the hcp peak disappear, yet diffraction peaks of long-range 18R type stacking order is not appreciable. The structure in this intermediate stage can be understood as a short-range stacking order. Such microstructure is possible because the introduction of stacking faults in the present process is not cooperative but rather described as a stochastic process driven by cluster distribution and thermally activated dislocation motion. The average stacking fault density close to that of the 18R is realized because the number density of clusters, or the amount of solute atoms available for the microstructure formation is equivalent to the 18R long-range order, but once a stacking fault is introduced by chance, it is persistent

and takes long time to change the position even if the distance between the neighboring stacking fault is less or more than 6 atomic planes. In much dilute alloys, formation of stacking faults/ and their extension in in-plane and out-of-plane directions have been examined by Kiguchi et al.[21] and Kim et al [23] by TEM/HAADF-STEM. They discussed the transition mechanism from GP zones / clusters into LPSO structures, and argued that the introduction of stacking faults and motion of Shockley partial dislocations may drive growth of LPSO. Their picture is consistent with the present case in that the transition is driven by independent dislocation motion.

3.2 Cluster growth and structural transition.

Figure 5 gives the change in the average radius obtained by Guinier approximation [25] as a function of annealing time including heating process. The samples are heated at the heating rate of 10 K/min. and then followed by an isothermal annealing. Small clusters with the average radius of 0.12 nm are found in the amorphous ribbons [17], then at the crystallization temperature, T_x, the size increased to approximately 0.22 nm. This size corresponds to the clusters consisting of 2 or 3 atoms as estimated from first-principles atomic positions after relaxation [17] in hcp lattice. For the isothermal annealing at 583 K, i.e., above the bifurcation temperature, the average radius already increased to the size expected for the $L1_2$ cluster when the isothermal annealing started, therefore, the radius remained constant during the process. For the annealing below T_{bif}, the average radius is smaller than that for $L1_2$ clusters, and continues to increase still below the size of $L1_2$ cluster during annealing. The average radius after annealing at 524 K for 3.6 ks is about 0.28 nm, which is about 20 % smaller than that for $L1_2$ clusters, while the integrated intensity of 103 peak, Q_{103}, decreased to about a half as shown in Fig. 6. The change in the cluster radius during isothermal annealing below the bifurcation temperature suggests that introduction of the stacking faults and the growth of clusters occurred simultaneously, and therefore, the introduction of stacking faults does not necessarily wait until the average clusters size to grow to the size of $L1_2$ clusters as observed for the case of constant rate heating

[17]. Then a question arises whether the clusters trapped within the stacking faults are expected to have grown to $L1_2$ clusters. This point is discussed later in conjunction with the introduction of stacking faults. Present in-situ measurements for isothermal annealing shows that the clustering and introduction of stacking faults occur concomitant below the bifurcation temperature. Figure 6 compares an example of the temporal decay of the integrated intensity of 103 peak and the temporal increase of 112 peak during the heat treatment with the isothermal temperature of 524 K. The initial decay rate of Q_{103} in the isothermal process may be evaluated by an exponential form as described as ;

$$Q_{103}(t)=Q_0 \exp(-t/\tau)$$

where τ is a characteristic decay time. Figure 6 shows that the approximation holds up to about 0.7 ks after the isothermal process started, and then the decay gradually slowed down.

3.3 Evolution of spatial distribution of clusters.

Figure 7 shows the structure function, $S(q)$, defined as :

$$S(q)=I(q)/F^2(qR) \quad , \qquad (1)$$

where $I(q)$ is the cluster components of SAXS intensity, and $F(qR)$ is the average form factor of clusters with the size R. $S(q)$ reflects the spatial distribution of clusters, and useful to extract cluster arrangements when the size of the clusters also changes. Figure 7 shows that the solute clusters of the average size of 0.12 nm distribute with the inter cluster distance of about 1.25 nm. Upon crystallization, well-defined single peak was observed. After isothermal annealing, a small hump begins to grow at the scattering vector of 4 nm^{-1} < q < 5 nm^{-1} as shown by an arrow, while another peak grow and becomes sharper at q~ 6 nm^{-1}. Fig.7 suggests that the interlayer interference is weak for SR-SO microstructures, while that for LPSO, for example, the peak height at 673 K during constant rate heating, increases up to 3.5[17]. This result implies that the in-plane order develops earlier than interplane order once stacking faults are introduced.

3.4 Kinetics of structural transformation.

Since the driving force of the formation of LPSO structure contains a structural origin as shown by Iikubo et al.[20], and a chemical origin as shown by Masumoto et al.[26], these processes may proceed concomitantly or separately depending on the heat treatment conditions. In the solute lean samples such as $Mg_{97}Y_2Zn_1$ or $Mg_{98.5}Y_1Zn_{0.5}$, clusters, or GP zones in hcp lattice tend to form on a few basal segregation layers, which later transform into LPSO block structures after introduction of stacking faults[21]-[23], rather than uniformly dispersed in hcp matrix as observed in the concentrated alloys of $Mg_{85}Y_9Zn_6$ alloys. The schematic illustration for the transition depicted in [17] suggests that it is natural to assume that the randomly distributed clusters transformed to LPSO structure via formation of such segregated, i.e., densely populated stacking fault layers. The temporal decay of the integrated intensity of 103 diffraction peak, Q, is a good measure to evaluate degree of completion of the structural phase transformation. Figure 6 gives the change of Q for isothermal annealing temperature of 524 K as a function of time. The rate of transformation as measured by volume of hcp regions was estimated by a simple exponential form as,

$$Q(t,T) = Q_0 \exp(-t/\tau(T)) \qquad (2).$$

The characteristic decay time, τ, depends on the isothermal annealing temperature, T_i, as,

$$\tau(T) = \tau_0 \exp(Q_A/RT) \quad , \qquad (3)$$

because the process under isothermal annealing suggested that the structural transition is thermally activated with an activation energy of Q_A. Figure 7 shows the decay time, τ, as a function of 1/T. The decay time was evaluated for the temperatures between crystallization temperatures and the bifurcation temperatures to obtain activation energy. The plot shows a good linear relationship and the activation energy of 173.6 ±14.4 kJ/mol was obtained. Since the structural transformation during isothermal annealing accompany cluster growth and rearrangement or shearing of clusters, the origin of activation energy is related either to diffusion or to the activation energy of dislocation motion such as energy barrier appearing in generalized stacking fault energies. Concerning diffusion, the activation

energy of self / impurity diffusion in Mg are reported to be smaller, for example, 135 kJ/mol for Mg self diffusion, 120 kJ/mol for Zn in Mg [27,28], and 92~99 kJ/mol for Y in Mg [29]. For grain-boundary diffusion which plays an important role for creep deformation at elevated temperatures, the activation energy is even lower and estimated as 79~83 kJ/mol [30,31]. An alternative explanation may come from the activation energy required to displace the atoms in the segregation layers. Considering that the structural transformation is expected to occur by Shockley partial dislocations to go through the segregated layer, the energy barrier for such dislocation motion may be another candidate. However, no published results for the present condition is available at this moment. Published generalized stacking fault energy (GSFE) calculations using first principles [32,33] focused on how the energy barrier was lowered by addition of solute elements, aiming at better deformability. In the present case, however, the driving force for dislocation motion is not externally applied stress, but internal driving force of phase transition in the segregated layers. Further, the partial dislocations go through the atomic plane that are considered to be the hardest layer for deformation when the clusters exist on the planes. Therefore, interpretation of the present results requires the value for segregated layers, i.e., hard layers, where dislocations that convey plastic strain upon deformation never go through. Therefore, this approach remains open question now. If such value for segregated layers of MgYZn LPSO becomes available, we may examine if the activation energy of dislocation motion with similar treatment of pinning by clusters as that for kink motion is a reasonable explanation [34]. Although Fig.8 gives well-defined linear relationship to suggest single thermally activated process, effect of constant rate heating prior to the isothermal annealing on the Ahrenius plot need to be examined. Assuming that the rate equation of eqs. (2) and (3) hold for all the temperature range of interest, degree of phase transformation proceeded during heating is estimated by equivalent time normalized for the temperatures. The effect was examined by a model calculations using the activation energy of 174 kJ/mol and $\tau(T)$ obtained from Fig.8, and assuming that the driving force for

the transformation does not change in the present temperature range of interest, i.e., between Tx, and T_{bif}. Then the degree of phase transformation, $f(t^*_i)$, before the sample reached the isothermal annealing temperature, T_{iso}, is estimated by using t_i^* and $\tau(T)$, where t* is the equivalent annealing time normalized to the isothermal annealing temperature, defined by :

$$t^* = \int_{t0}^{t(T)} \exp(Q_A/RT_i) \,/\, \exp(Q_A/RT(t))\, dt \qquad (4)$$

and

$$f(t) = \exp(-t\, i^*/\tau(T(t)) \qquad . \qquad (5)$$

t_i^* is the time when the sample reached the isothermal annealing temperature, Ti, and $\tau(T)$ is the characteristic decay time obtained from Fig.8. f(t) is the fraction of the hcp crystals remained at time t, including the process of the constant rate heating. Figure 9 shows a temporal decay of the integrated intensity calculated from equations (4) and (5). The fraction of remained hcp when the sample temperature reached the isothermal temperature is shown by arrows for 550 K and 575K. It is seen that the integrated intensity of 103 peak should significantly decreased before the sample temperature reached the isothermal temperature above Tbif, while the decrease during heating is relatively small for $T_{iso}<T_{bif}$, and it should be reasonable to evaluate $\tau(T)$ from the slope as shown in Fig. 6. Figure 9 also explains why the well-defined transition temperature appeared in the constant rate heating process in the previous work [17].

Exponential decay of the integrated intensity holds in the early stage after reaching the isothermal annealing temperatures for all the experimental condition below T_{bif}. On the other hand, the simple rate equation of eq.(2) may be generalized as a Kormogorv-Johonson-Mehl-Avrami (KJMA) equation as ;

$$1 - Q(r,T)/Q_0 = \exp\{-(\alpha\, t)^m\} \qquad (6)$$

where m is the Avrami exponent and α is a rate parameter related to a thermal activation process as

$$\alpha = A \exp(-Q_A/kT) \,. \qquad (7)$$

The fitting results on the integrated intensity of 103 peak gave 0.65 ± 0.1 for m and 175±25 kJ/mol for Q_A, that is, the introduction process of stacking faults in LPSO alloys is fitted by KJMA scheme with the exponent m less than 1.0, suggesting that a simple grain growth model, regardless of whether it is one dimensional growth or two dimensional one, does not explain the results. Although the activation energy obtained by the KJMA approach is more scattered than a simple exponential analysis, the values agree within the estimated error. Therefore, we may use the energy to examine the relationships between the introduction of stacking faults and the growth of clusters at different isothermal annealing temperatures.

3.5 Relationship between cluster growth and introduction of stacking faults

The relationship between the cluster growth and the introduction of stacking faults was examined by plotting the cluster size as a function of time normalized by the activation energy obtained for eq. (3), i.e., degree of introduction of stacking faults. Figure 10 shows the relationship between the average size of clusters and time normalized by the characteristic time for the introduction of stacking faults. The figure suggests that the growth and maturation of $L1_2$ clusters occur concomitant with the introduction of stacking faults for a wide range of annealing temperatures, and the degree of maturation is strongly correlated with the degree of structural transformation. Model B assumes that all the clusters trapped by the stacking faults are the $L1_2$ clusters, while those in hcp crystal region remain the initial size. Assuming that fraction of clusters trapped in the stacking faults is equal to the fraction of stacking faults against necessary number of stacking faults for LPSO formation, overestimation of model B suggests that some part of the clusters trapped in the stacking faults are still smaller than the $L1_2$ cluster. In the model A, it is assumed that x% of the clusters are still as small as that in hcp, i.e., 0.25 nm, and the rest grows to $L1_2$ cluster with 0.35 nm, with x decrease from 70 at $\tau<=0.5$ to 0.1 at $\tau>2$ as shown in the figure, with the statistical averaging of the Guinier radius defined by, $Rs^2=<R^8>/<R^6>$ [35]. Since model A uses the lower limit of estimates of the size of

immature cluster, and model B gives the upper limit of the fraction of immature clusters in the stacking faults, this simple estimation suggests that in the early stage of introduction of stacking faults, large fraction of clusters in the stacking faults are still smaller than the $L1_2$ cluster size, but once captured in the stacking faults, they are allowed to grow up to the size of $L1_2$ clusters.

4.Summary

In summary, in-situ small and wide angle scattering measurements of liquid-quenched amorphous $Mg_{85}Y_9Zn_6$ alloy ribbons during isothermal annealing have been performed utilizing synchrotron radiation. It is shown that the introduction of the stacking faults is a thermally activated process with the activation energy of 173.6±14.4 kJ/mol. Formation of LPSO at lower temperatures suggests dense but random nucleation of stacking faults, leading to 18R spacing as an average. Still, the sample gives no clear diffraction peak for the perfect 18R stacking periodicity in a crystallographic sense. We may call this transient microstructure as short range stacking ordered (SR-SO) structure or average period stacking ordered structure that is a transient nonequilibrium microstructure, instead of long period stacking ordered structure. Understanding the stability and characteristics of this microstructure may help developing lighter Mg alloys with lower solute addition, with introduction of randomly and more sparsely segregated YZn cluster layers.

Acknowledgments

This work was supported by Grant-in-Aid for Scientific Research from JSPS, grant number 16H04492 and innovative research area, 18H05476 and from Light Metal Education Foundation. In-situ synchrotron radiation measurements were performed under proposal numbers 2017G593 at Photon Factory and 2017A1437, 2018A1206 and 2018B1230 of Spring8.

REFERENCES

[1] Y. Kawamura, K.Hayashi, A. Inoue, T. Masumoto, Rapidly Solidified Powder Metallurgy $Mg_{97}Zn_1Y_2$ Alloys with Excellent Tensile Yield Strength above 600 MPa, Mater. Trans. **42** (2001) 1172-1176.

[2] T. Itoi, T. Semiya, Y. Kawamura, M. Hiroshashi, Long period stacking structures observed in $Mg_{97}Zn_1Y_2$ alloy, Scr. Mater. **51** (2004) 107-111. doi:10.1016/j.scriptamat.2004.04.003

[3] M. Yamasaki, M. Sasaki, M. Nishijima, K. Hiraga, Y. Kawamura, Formation of 14H long period stacking ordered structure and profuse stacking faults in Mg-Zn-Gd alloys during isothermal aging at high temperature, Acta Mater. **55** (2007) 6798-6805. doi:10.1016/j.actamat.2007.08.033

[4] Y. M. Zhu, A. J. Morton, J.F. Nie, The 18R and 14H long-period stacking ordered structures in Mg-Y-Zn alloys, Acta Mater. **58** (2010) 2936-2947. doi:10.1016/j.actamat.2010.01.022

[5] K. Hagihata, N. Yokotani, Y. Umakoshi, Plastic deformation behavior of Mg12YZn with 18R long-period stacking ordered structure, Intermetallics **18** (2010) 267-276. doi:10.1016/j.intermet.2009.07.014

[6] Y. Kawamura, M. Yamasaki, Formation and Mechanical Properties of Mg97Zn1RE2 Alloys with Long-Period Stacking Ordered Structure, Mater. Trans. **48** (2007) 2986-2992.

[7] H. Yokobayashi, K. Kishida, H. Inui, M. Yamasaki, Y. Kawamura, Enrichment of Gd and Al in the quadruple close packed planes and their in-plane long-range ordering in the long period stacking-ordered phase in the Mg-Al-Gd system, Acta Mater. **59** (2011) 7287-7299. doi:10.1016/j.actamat.2011.08.011

[8] D. Egusa, E. Abe,The structure of long period stacking/order Mg-Zn-RE phases with extended non-stoichiometry ranges, Acta Mater. **60** (2012) 166-178. doi:10.1016/j.actamat.2011.09.030

[9] K.Kishida, H.Yokobayashi, H.Inui,A formation criterion for Order-Disorder(OF) phases of the Long Period Stacking Order (LPSO)-type 院 Mg-Al-RE(Rare Earth) Ternary Systems, Sci. Reports **7** (2017) 12294. DOI:10.1038/s41598-017-12506-0

[10] E. Saal, C. Wollverton, Thermodynamic stability of Mg-based ternary long-period stacking ordered structures, Acta Mater. **68** (2014) 325-338. DOI：10.1016/j.actamat.2013.10.055

[11] H. Kimizuka, M. Fronzi, S. Ogata, Effect of alloying elements on in-plane ordering and disordering of solute clusters in Mg-based long-period stacking ordered structures; A first-principles analysis, Scr. Mater. **69**(2013)594-597. DOI：10.1016/j.scriptamat.2013.07.003

[12] J. Grobner, A .Kozlov, X.Y. Feng, J. Geng, J.F. Nie, R. Schimid-Fetzer, Phase equilibria and transformation in ternary Mg-rich Mg-Y-Zn alloys, Acta Mater. **60** (2012) 5948-5962. DOI：10.1016/j.actamat.2012.05.035

[13] S. Minamoto, S. Nomoto, A. Hamaya, T. Horiuchi, S. Miura, Microstructure Simulation for Solidification of Magnesium-Zinc-Yttrium Alloy by Multi –phase –field Method Coupled with CALPHAD Database, ISIJ Intern. **50** (2010) 1914-1919.

[14] M. Yamasaki, M. Matsushita, K. Hagihara, H. Izuno, E. Abe, Y. Kawamura, Highly ordered 10H-type long-period stacking order phase in a Mg-Zn-Y ternary alloy, Scr. Mater. **78-79** (2014) 13-16. DOI：10.1016/j.scriptamat.2014.01.013

[15] K.Kishida, K.Nagai, A.Mtsumoto, A.Ysuhara, H.Inui, Crystal structures of highly-ordered long-period stacking –ordered phases with 18R,14H and 10H-type stacking sequences in the Mg-Zn-Y system, Acta Mater. **99** (2015) 228-239. DOI：10.1016/j.actamat.2015.08.004

[16] H.Okuda, K.Kintsu, M. Ito, M.Yamasaki, Y.Kawamura, in preparation.

[17] H.Okuda, M.Yamasaki, Y.Kawamura,M.Tabuchi, H.Kimizuka, Nanoclusters first; a hierarchical phase transformation in a novel Mg alloy, Sci. Rep. **5** (2015) 14186. DOI: 10.1038/srep14186

[18] H.Okuda, H.Tanaka, S.Shiratake, M.Yamasaki, Y.Kawamura, Development of microstructures in rapidly-quenched Mg85Y9Zn6 alloy ribbons during heating at a constant speed examined by simultaneous small- and wide angle scattering measurements, Acta Mater. **118** (2016) 95-99. DOI:10.1016/j.actamat.2016.06.028

[19] H. Okuda, M. Yamasaki, Y. Kawamura, Transition to long period stacking ordered structures in $Mg_{85}Gd_9Zn_6$ alloys from amorphous ribbons examined by synchrotron radiation scattering: Comparison with $Mg_{85}Y_9Zn_6$ alloys, Scr. Mater. **137** (2017) 26-29. DOI:10.1016/j.scriptamat.2017.06.013

[20] S. Iikubo, K. Matsuda, H. Ohtani, Phase stability of long-period stacking structures in Mg-Y-Zn: A first-principles study, Phys. Rev. B86(2012)054105. DOI: 10.1103/PhysRevB.86.054105

[21] S. Matsunaga, T. Kiguchi, K. Sato, T. J. Konno, Local Strain Fields of LPSO in Mg-Based Ternary Alloys, Mater. Trans. **56** (2015) 923-927. doi:10.2320/matertrans.MH201404

[22] T. Kiguchi, Y. Ninomiya, K. Shimmi, K. Sato, T.J. Konno, Structural and Compositional Modulation in Transformation of LPSO structure in Mg97Zn1Y2 Cast Alloys, Mater. Trans. **54** (2013) 668-674. doi:10.2320/matertrans.MI201221

[23] J.K. Kim, L. Jin, S. Sandloebes, D. Raabe, Diffusional-displacive transformation enables formation of long-period stacking order in magnesium, Sci. rep. **7** (2017) 4046. DOI:10.1038/s41598-017-04343-y

[24] H.Okuda,T.Horiuchi, S.Ochiai, M.Yamasaki, Y.Kawamura, Evolution of long-period stacking order structures on annealing as-cast Mg85Y9Zn6 alloy ingot observed by synchrotron radiation small-angle scattering, Scr. Mater. **68** (2013) 575-778. DOI:10.1016/j.scriptamat.2012.11.041

[25] A. Gunier, G. Fournet, Small-angle scattering of X-rays, John Wiley & Sons, NewYork. 1955.

[26] R. Masumoto, H. Ohtani, M. Hasebe, Thermodynamic Analysis on the Phase Separation of hcp Phase in the Mg-Y-Zn Ternary System, J. Jpn. Inst. Metals **73** (2009) 683-690 .[in Japanese]

[27] P.G. Shewmon, Self-Diffusion in Magnesium Single Crystals, Trans. AIME **206** (1956) 918-922.

[28] J. Cemak, I. Stloukal, Diffusion of ^{65}Zn in Mg and Mg-xAl solid solutions, Phys. Stat. Solidi A**203** (2006) 2386-2392. DOI 10.1002/pssa.200622219

[29] S.K.Das, Ph.D thesis submitted to McGill University, 2014.

[30] A.M. Brown, M.F. Ashby, Correlations for Diffusion Constants, Acta Metall. **28**(1980)1085-1101.

[31] W. Gust, S. Meyer, A. Bogel, B. Predel, Generalized representation of grain boundary self-diffusion data, J. Phys. **46** C4 (1985) 537. 2202. DOI:10.1051/jphyscol:1985460

[32] T. Tsuru, Y. Udagawa, M. Yamaguchi, M. Itakura, H. Kaburaki, Y. Kaji, Solution softening in magnesium alloys; the effect of solid solutions on the dislocation core structure and nonbasal slip, J.Phys. Cond. Matter **25** (2013)022202. doi:10.1088/0953-8984/25/2/022202

[33] K.H.Kim, J.H.Hwang, H-S. Jeon, J.B.Jeon, N.T. Kim, B-J. Lee, Dislocation binding as an origin for the improvement of room temperature ductility in Mg alloys, Mater. Sci. Engineering, A **715** (2018) 266-275. DOI:10.1016/j.msea.2018.01.010

[34] J. Lothe, J.P. Hirth, Dislocation Dynamics at Low Temperatures, Phys. Rev. **115** (1959) 543-550.

[35] V. Gerold, in *Small-angle scattering*, ed. H. Brumberger, Gordon & Breach, New York, 1965, pp277-318.

Figure Captions

Fig.1 Small and Wide-angle X-ray scattering (SWAXS) profile during in-situ heating of amorphous Mg85Y9Zn6 ribbons at 10 K/min. At the crystallization temperature, diffuse hcp 103 peak appeared in WAX profile, and disappear at the bifurcation temperature, T_{bif}, when the well-defined SAX peak between 4 nm^{-1} and 6 nm^{-1} started to split into in-plane and interplane peaks at higher temperature. T_{bif} was experimentally obtained from the integrated intensity of 103 Bragg peak for the constant rate heating of 10 K/min.as shown in the bottom.

Figure 2. Temperature diagram used in the present in-situ SWAXS measurements.

Figure 3. Small- and wide- angle scattering /diffraction profiles during in-situ heating. Previous work of 10 K/min. heating up to melting point shows a well-defined bifurcation of the SAXS peak. Present isothermal in-situ measurements examine the temporal transformation kinetics at the temperatures between Tx and Tbif, where the SAXS peak does not show a well-defined bifurcation, still noticeable decrease in hcp 103 peak was observed. The pattern in the upper left of the figure shows the positions of peaks calculated for 18R-LPSO and hcp solid solution alloys with the same lattice spacing as LPSO using crystallographic data. The peaks shown by the red diamonds are observed for well-defined periodicity of stacking, and did not appear even for long time annealing in low-temperature isothermal annealing as shown in the right side of the figure.

Figure 4. Change of SAXS and WAXD patterns during isothermal heat treatment at 510 K. The sample was heated to 510 K at 10 K/min. first, and then isothermal annealing was made.

Figure 5. Evolution of cluster radius during heat treatments. It should be noted that the radius is still far smaller than that for L12 clusters even after long-time annealing of 4ks, while clear decay in 103

Bragg peak was observed.

Figure 6. Temporal decay of the integrated intensity of 103 Bragg peak for the isothermal annealing at 524 K. For the regions where both hcp and LPSO peaks may appear, the integrated intensity in turn increase with time.

Figure 7 Structure function for T_{iso}=524 K. During heating, the structure function gave a single peak form. During succeeding isothermal annealing, the structure function gradually shows another weak convex part at a q between 4 nm^{-1} and 5 nm^{-1}.

Figure 8. Characteristic decay time for hcp 103 peak as a function of isothermal annealing temperature. An activation energy of 173.6 ± 14.4 kJ/mol was obtained for the temperatures between the bifurcation temperature and the crystallization temperature.

Figure 9 Temporal decay of hcp peak calculated from equation 4 and 5. The effect of transformation before the sample reaches the isothermal temperature is limited below Tbif, while the integrated intensity decreased significantly for T_{iso} above T_{bif}. The activation energy of 174 kJ/mol was used for the calculation.

Figure 10 Evolution of cluster size during isothermal process plotted against elapsed time from the onset of crystallization, normalized by the characteristic time for introduction of stacking faults, τ(T). The increase in the radius is overestimated assuming that all the clusters in the stacking faults are always the $L1_2$ clusters as shown in model B.

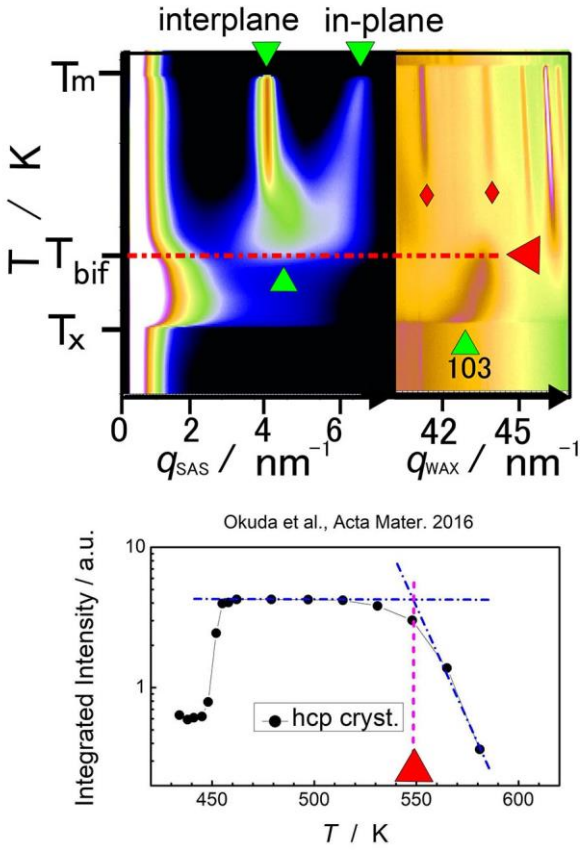

Fig.1 Small and Wide-angle X-ray scattering (SWAXS) profile during in-situ heating of amorphous Mg85Y9Zn6 ribbons at 10 K/min. At the crystallization temperature, diffuse hcp 103 peak appeared in WAX profile, and disappear at the bifurcation temperature, T_{bif}, when the well-defined SAX peak between 4 nm^{-1} and 6 nm^{-1} started to split into in-plane and interplane peaks at higher temperature. T_{bif} was experimentally obtained from the integrated intensity of 103 Bragg peak for the constant rate heating of 10 K/min.as shown in the bottom.

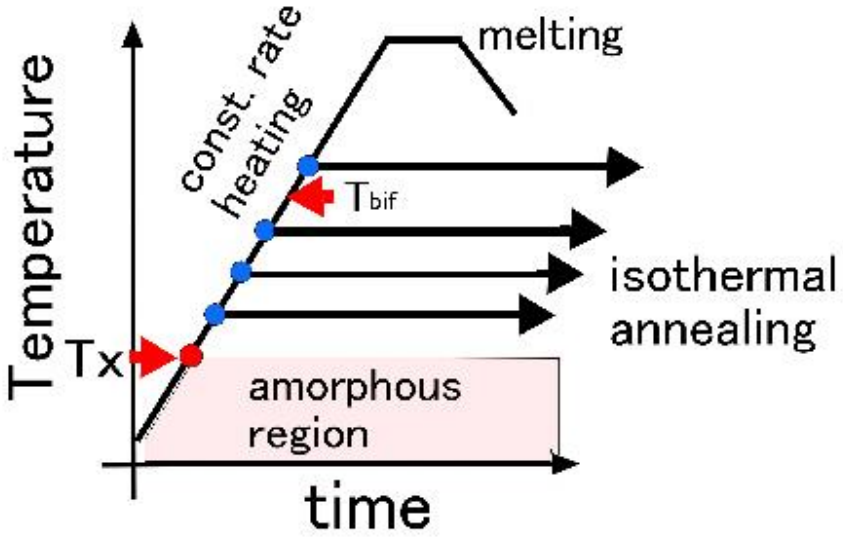

Figure 2 Temperature diagram used in the present in-situ SWAXS measurements.

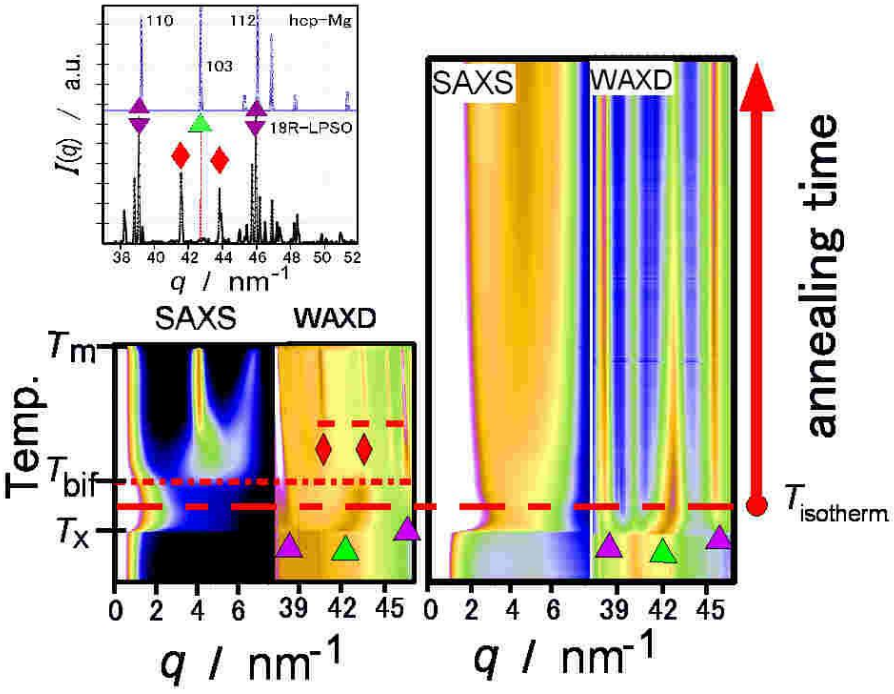

Figure 3. Small- and wide- angle scattering /diffraction profiles during in-situ heating. Previous work of 10 K/min. heating up to melting point shows a well-defined bifurcation of the SAXS peak. Present isothermal in-situ measurements examine the temporal transformation kinetics at the temperatures between T_x and $T_{bif,}$ where the SAXS peak does not show a well-defined bifurcation, still noticeable decrease in hcp 103 peak was observed. The pattern in the upper left of the figure shows the positions of peaks calculated for 18R-LPSO and hcp solid solution alloys with the same lattice spacing as LPSO using crystallographic data. The peaks shown by the red diamonds are observed for well-defined periodicity of stacking, and did not appear even for long time annealing in low-temperature isothermal annealing as shown in the right side of the figure.

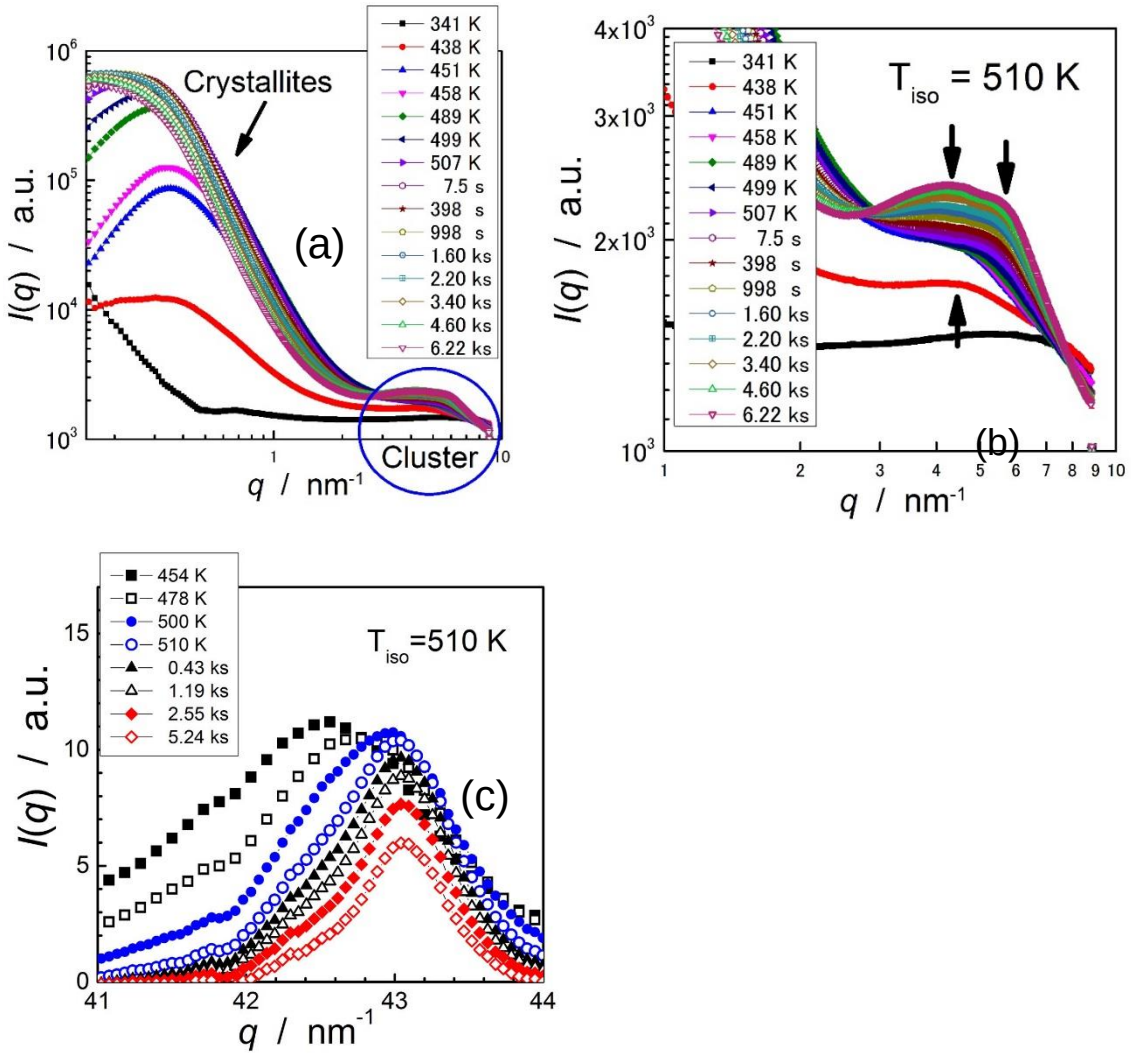

Figure 4. Change of SAXS and WAXD patterns during isothermal heat treatment at 510 K. The sample was heated to 510 K at 10 K/min. first, and then isothermal annealing was made.

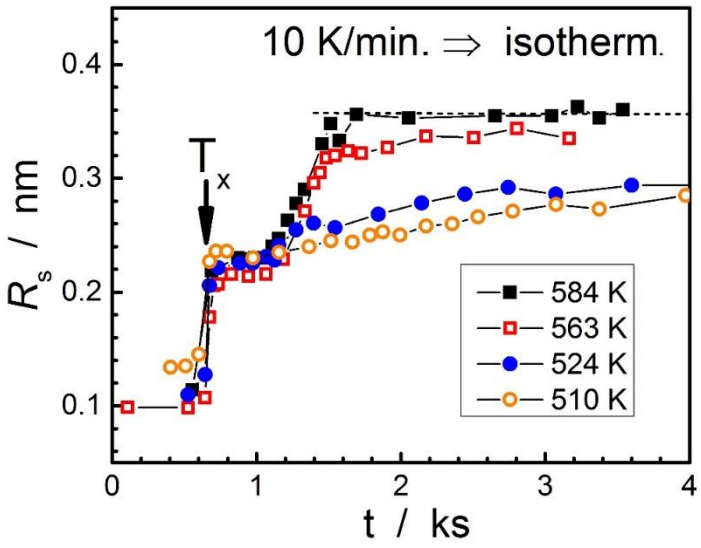

Figure 5. Evolution of cluster radius during heat treatments. It should be noted that the radius is still far smaller than that for $L1_2$ clusters even after long-time annealing of 4ks, while clear decay in 103 Bragg peak was observed.

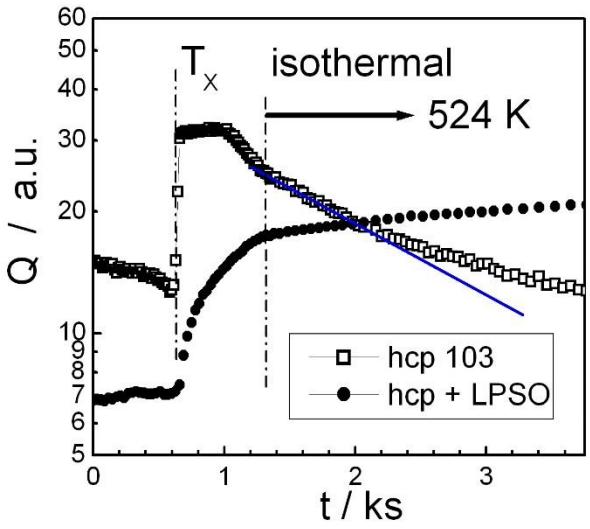

Figure 6. Temporal decay of the integrated intensity of 103 Bragg peak for the isothermal annealing at 524 K. For the regions where both hcp and LPSO peaks may appear (37.8 nm^{-1}<q<39.1 nm^{-1}), the integrated intensity in turn increase with time.

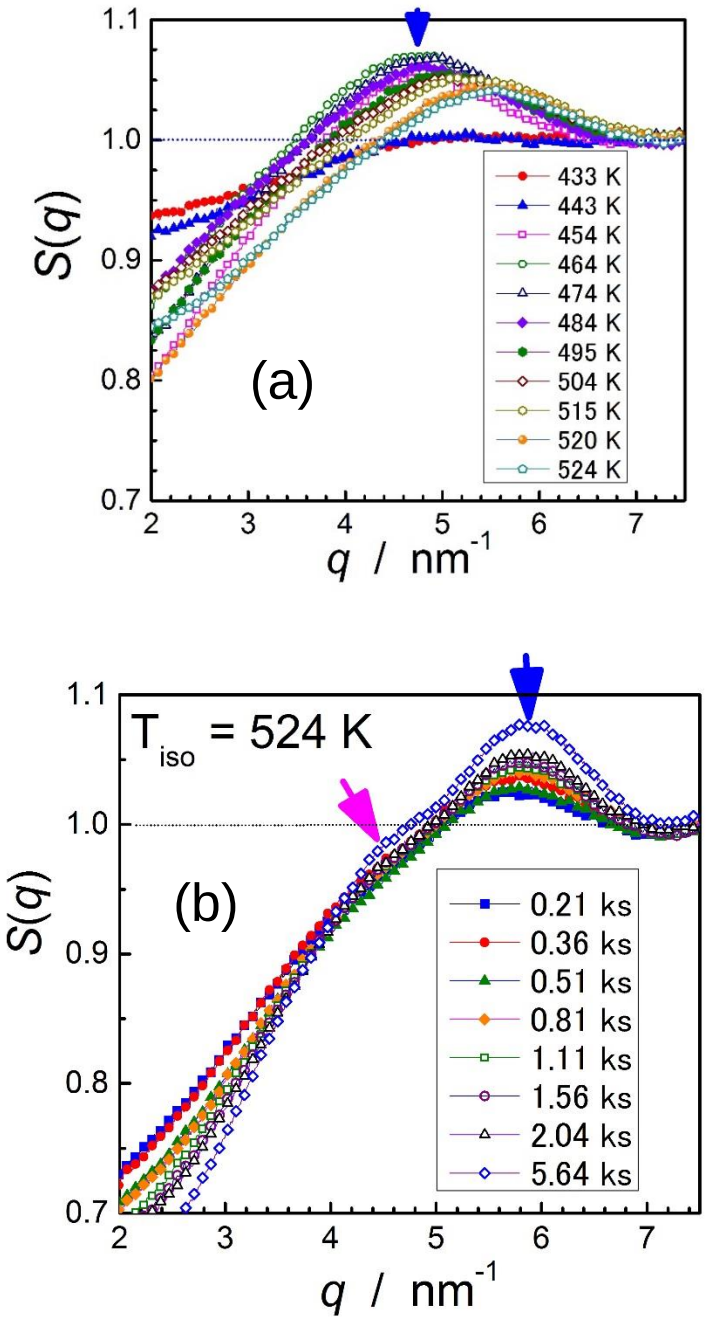

Figure 7 Structure function for Tiso=524 K. During heating, structure functions gave a single peak form. During succeeding isothermal annealing, the structure function gradually shows another weak peak at a q between 4 nm^{-1} and 5 nm^{-1}.

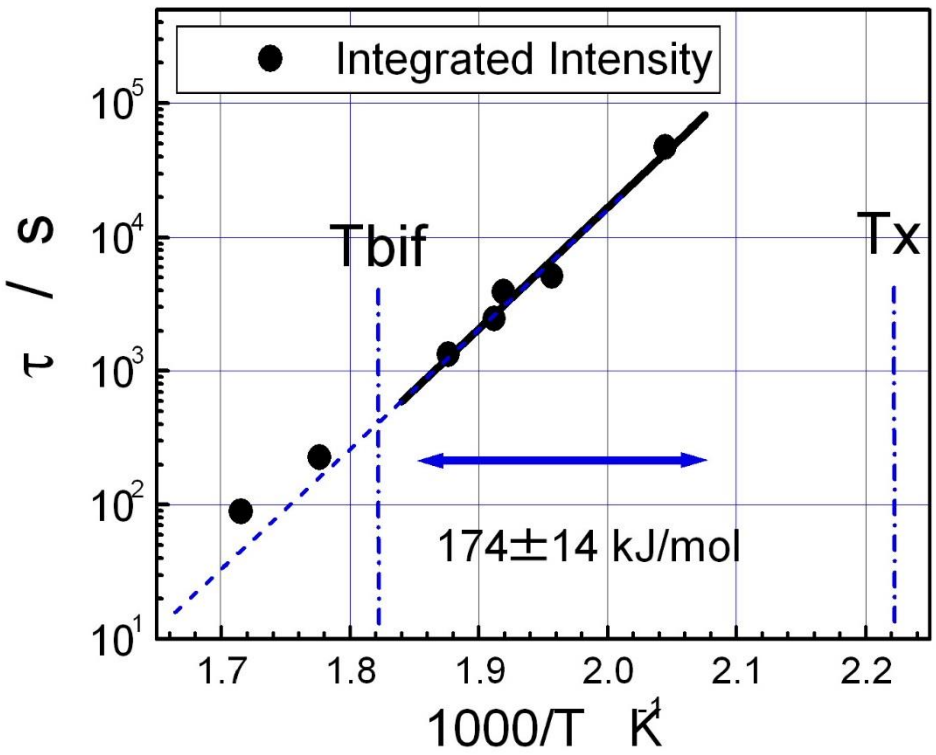

Figure 8. Characteristic decay time for hcp 103 peak as a function of isothermal annealing temperature. An activation energy of 173.6 ± 14.4 kJ/mol was obtained for the temperatures between the bifurcation temperature and the crystallization temperature.

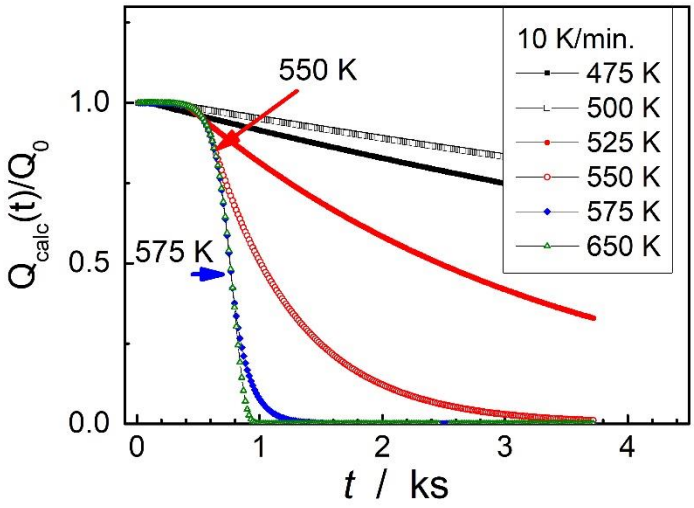

Figure 9 Temporal decay of hcp peak calculated from equations 4 and 5. The effect of transformation before the sample reaches the isothermal temperature is limited below T_{bif}, while the integrated intensity decreased significantly for T_{iso} above $T_{bif.}$ The activation energy of 174 kJ/mol was used for the calculation..

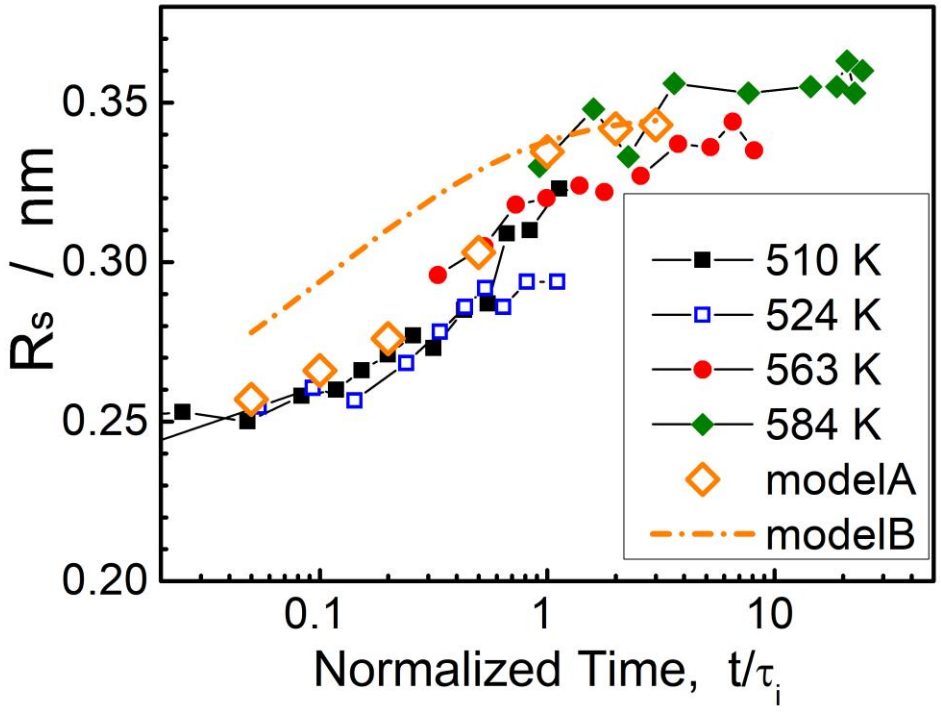

Figure 10 Evolution of the cluster size during isothermal process plotted against elapsed time from the onset of crystallization, normalized by the characteristic time for introduction of stacking faults, τ(T). The increase in the radius is overestimated assuming that all the clusters in the stacking faults are always the $L1_2$ clusters as shown in model B.